

Temporally Varying Mesoscale Eddy Characteristics in the California Current System Identified from RAFOS Floats

Peter C Chu^{1,*}, Chenwu Fan¹

¹ Department of Oceanography, Naval Postgraduate School, Monterey, CA 93943, USA

* Corresponding author: pcchu@nps.edu

ABSTRACT

The SOund Fixing And Ranging (RAFOS) floats were deployed by the Naval Postgraduate School (NPS) near California coast from 1992 to 2004 at depth between 150 and 600 m (<http://www.oc.nps.edu/npsRAFOS/>). Each drifter trajectory is adaptively decomposed using the empirical mode decomposition (EMD) into low-frequency (non-diffusive, i.e., current) and high-frequency (diffusive, i.e., eddies) components. The identified eddies are mostly anticyclonic with total 203 anticyclonic and 36 cyclonic spirals. Eddy characteristics are determined from the time series of individual RAFOS float trajectory. They are the current velocity scale, eddy radial scale, eddy velocity scale, eddy Rossby number, and eddy-current kinetic energy ratio. The California Current System is found an eddy-rich system with the overall eddy-current kinetic energy ratio of 1.78. It contains submesoscale and mesoscale eddies. The horizontal length scale of 10 km is a good threshold of the eddy radial scale (Leddy) to separate the two kinds of eddies. The mean eddy Rossby number is 0.72 for the submesoscale eddies and 0.06 for the mesoscale eddies. The current-eddy kinetic energy ratio is similar between submesoscale and mesoscale eddies. This may imply similar current-eddy kinetic energy transfer for submesoscale and mesoscale eddies. Statistical characteristics and interannual variability of current velocity scale and eddy characteristic parameters are also presented.

Descriptors: Empirical mode decomposition, Eddy radial scale, Eddy velocity scale, Eddy rossby number, Eddy-current kinetic energy ratio.

INTRODUCTION

The California Current system is one of the most productive and well-studied eastern boundary upwelling systems with high mesoscale activity, frequent formation of eddies, fronts, and filaments throughout the year. Numerous mesoscale eddies are generated by surface and subsurface currents. Cyclonic eddies are mainly generated at the surface with a surface core (in the upper 150 m), whereas anticyclonic eddies are predominantly

generated at subsurface with a subsurface core (~400 m) (Simpson and Lynn, 1990; Huyer et al., 1998; Collins et al, 1996, 2000; Garfield et al., 1999).

Trajectories of a set of N Lagrangian drifters at time t are represented by $\{\mathbf{x}^{(n)}(t) = [x^{(n)}(t), y^{(n)}(t)], \mathbf{u}^{(n)}(x, y, t), n = 1, 2, \dots, N\}$ with (x, y) the horizontal position. They measure fluid characteristics along fluid particles' trajectories (i.e., Lagrangian trajectories), and make water masses distinguishable in terms of origin and/or destination and traced, while its characteristics are continually changing. Eulerian velocity field can be calculated from Lagrangian trajectories using routine ocean data assimilation systems such as the optimal spectral decomposition (OSD) [Chu et al., 2003 a,b].

Submitted: 26-July-2021

Approved: 18-May-2022

Associate Editor: Ilson Silveira



© 2022 The authors. This is an open access article distributed under the terms of the Creative Commons license.

Some phenomena were identified such as fall–winter recurrence of current reversal from westward to eastward on the Texas–Louisiana continental shelf from near surface drifting buoy and current meter [Chu et al. 2005], and propagation of long baroclinic Rossby waves at mid-depth (around 1,000 m deep) in the tropical north Atlantic from the Argo floats (Chu et al. 2007).

Three major approaches are available to identify dynamic characteristics of currents and eddies from Lagrangian drifters without using ocean data assimilation: (a) particle dispersion, (b) Eulerian mean velocity, and (c) empirical mode decomposition. The first approach is the particle dispersion relative to their center,

$$X(t) = \frac{1}{N} \sum_{n=1}^N x^{(n)}(t), \quad Y(t) = \frac{1}{N} \sum_{n=1}^N y^{(n)}(t). \quad (1)$$

The variances of locations of N drifters at time instance t ,

$$D_x(t) = \frac{1}{N} \sum_{n=1}^N [x^{(n)}(t) - X(t)]^2, \quad D_y(t) = \frac{1}{N} \sum_{n=1}^N [y^{(n)}(t) - Y(t)]^2 \quad (2)$$

estimate the dispersion of the drifters [e.g., Obuko and Ebbesmeyer, 1976; Rypina et al., 2012]. The 2D turbulent diffusivities (K_x, K_y) are defined by

$$K_x = \frac{1}{2} \frac{\partial D_x}{\partial t}, \quad K_y = \frac{1}{2} \frac{\partial D_y}{\partial t} \quad (3)$$

With (D_x, D_y) grow linearly with time and the corresponding constant spreading rates (K_x, K_y) are referred as the 2D turbulent diffusivity of eddies [Rypina et al. 2012].

The second approach is to estimate the Eulerian mean velocity from a group of N drifters:

$$\mathbf{U}(x, y) = \langle \mathbf{u}^{(n)}(x, y, t) \rangle,$$

and subtraction of $\mathbf{U}(x, y)$ from the velocity identified from Lagrangian drifters, $\mathbf{u}^{(n)}(x, y, t)$, leads to the “residue” velocities,

$$\mathbf{u}_{res}^{(n)}(x, y, t) = \mathbf{u}^{(n)}(x, y, t) - \mathbf{U}(x, y). \quad (4)$$

Here, the Eulerian mean velocities are computed as an ensemble average in the defined

geographic region that velocities from different floats and times [e.g., Davis 1991; Collins et al., 2004; Chu et al., 2007; Chu and Fan, 2014] or as binned velocities with cubic splines [Bauer et al., 1998].

Both particle dispersion and Lagrangian residue velocities need sufficient number (N) of drifters in the calculation at then same time t . If there is very few co-deployed drifters such as less than three SOund Fixing And Ranging (RAFOS) floats available at same time-periods by the Naval Postgraduate School (NPS) in the California coasts (see website: <http://www.oc.nps.edu/npsRAFOS/>)? One option is to combine drifters from different time-periods together as if they were deployed at the same time-period. Such treatment cannot identify temporal variability of eddy characteristics.

The third approach is to use the empirical mode decomposition (EMD) (Huang et al. 1998) to separate a Lagrangian trajectory $\mathbf{x}(t)$ into deterministic [low frequency mode representing the currents, $\mathbf{x}_{cur}(t)$] and stochastic [non-low frequency mode representing eddy, $\mathbf{x}_{eddy}(t)$] trajectories (Chu 2018)

$$\mathbf{x}(t) = \mathbf{x}_{cur}(t) + \mathbf{x}_{eddy}(t), \quad (5)$$

where $\mathbf{x}(t)$ is the position vector at time t . This method is called the *deterministic-stochastic EMD*. The Lagrangian velocity is calculated by

$$\mathbf{u} = \frac{d\mathbf{x}(t)}{dt}, \quad \mathbf{u}_{cur} = \frac{d\mathbf{x}_{cur}(t)}{dt}, \quad \mathbf{u}_{eddy} = \frac{d\mathbf{x}_{eddy}(t)}{dt}. \quad (6)$$

Such Lagrangian-type decomposition changes the traditional approaches (particle dispersion and Lagrangian mean) of using N drifters [$\mathbf{x}^{(n)}(t), n = 1, \dots, N$] to get currents (i.e., mean flow) and eddies from Lagrangian trajectory data. The trajectories of 54 RAFOS floats deployed near California coast by C.A. Collins of the Naval Postgraduate School from 1992 to 2004 at depth between 150 and 600 m (<http://www.oc.nps.edu/npsRAFOS/>) (Fig. 1) show combination of deterministic (low frequency) and stochastic (high frequency) components.

This paper uses the deterministic-stochastic EMD to separate current and eddy from a single

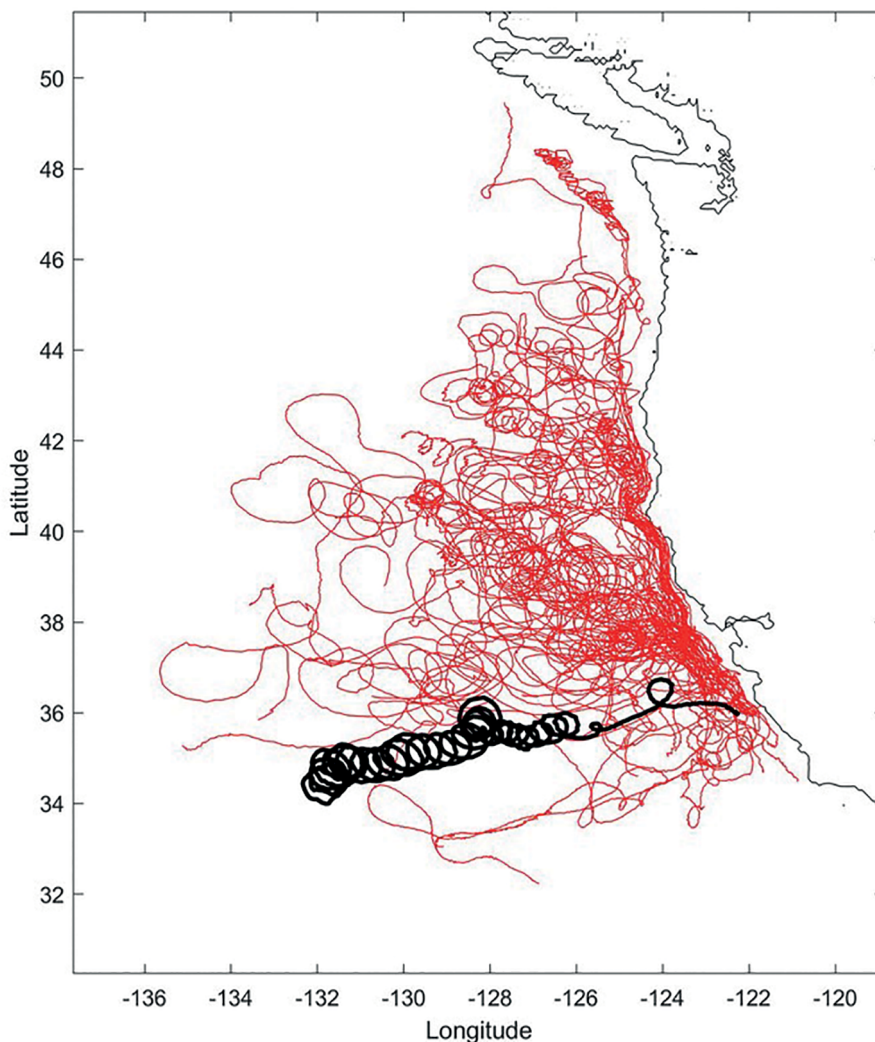


Figure 1. Trajectories of 54 RAFOS floats in the California coast by the Naval Postgraduate School between 1992 and 2004 (<http://www.oc.nps.edu/npsRAFOS/>). The thick black trajectory is the Float N073.

Lagrangian drifter. This procedure gives current velocity scale as well as eddy characteristic parameters such as the eddy radial scale, eddy velocity scale, eddy Rossby number, and eddy-current kinetic energy ratio. The rest of the paper is organized as follows. Section 2 describes the procedure of the deterministic-stochastic EMD. Section 3 and 4 present the identified current and eddy characteristic parameters for each RAFOS float and their statistics for 54 RAFOS floats. Section 5 describes the temporal variability of the current and eddy characteristic parameters. Section 6 presents the results.

DETERMINISTIC-STOCHASTIC EMD

The EMD (see Appendix A) decomposes a Lagrangian trajectory into the intrinsic mode functions (IMFs) regardless of their linearity, stationarity, and stochasticity (Huang et al., 1998; Chu et al., 2012, 2014). The key point to perform this decomposition is the sifting process (with four steps), which decomposes a Lagrangian drift trajectory $\mathbf{x}(t)$ into [see (A5) in Appendix A],

$$\mathbf{x}(t) = \sum_{p=1}^P \mathbf{x}_p(t) + \mathbf{r}(t) \quad (7)$$

where $\mathbf{x}_p(t) = [x_p(t), y_p(t)]$, is the p -th IMF and $\mathbf{r}(t) = [r_x(t), r_y(t)]$ is the trend (no oscillation). The first IMF

has highest frequency, and frequency reduces as the subscript p increases. The trajectory data from the RAFOS float #N073 is used for illustration and represented as a thick curve in Fig. 1, downloaded from <http://www.oc.nps.edu/npsRAFOS/DATAS/NPS035/DATAS.html>. The data were collected by Professor C.A. Collins at the Naval Postgraduate School). The data are represented by time series of horizontal position vector, $\mathbf{x}(t) = [x(t), y(t)]$, with x in the zonal direction, and y in the latitudinal direction.

The RAFOS subsurface data downloaded from <http://www.oc.nps.edu/npsRAFOS/> contains 61 RAFOS floats. Among them 7 floats (N001, N009, N012, N042, N046, N049, N068) have too many

missing data inside the time series. They are not included in the computation. The date rate varies from general 3/day to around 22/day (N030 18 May – 10 June 1994). For each float, the time series $[x(t), y(t)]$ are decomposed into IMFs and trend using the EMD method (see Appendix A). Seven IFMs and a trend are identified in the (x, y) directions (Fig. 2). It clearly shows that the high frequency motion dominates the low IFM modes. Frequency reduces as the IFM mode from the lowest (IMF-1) to the highest (IMF-7). The trend (no oscillation) is of course the part of the deterministic motion, but not all.

The IMFs are separated into the deterministic and stochastic parts, using the steepest ascent

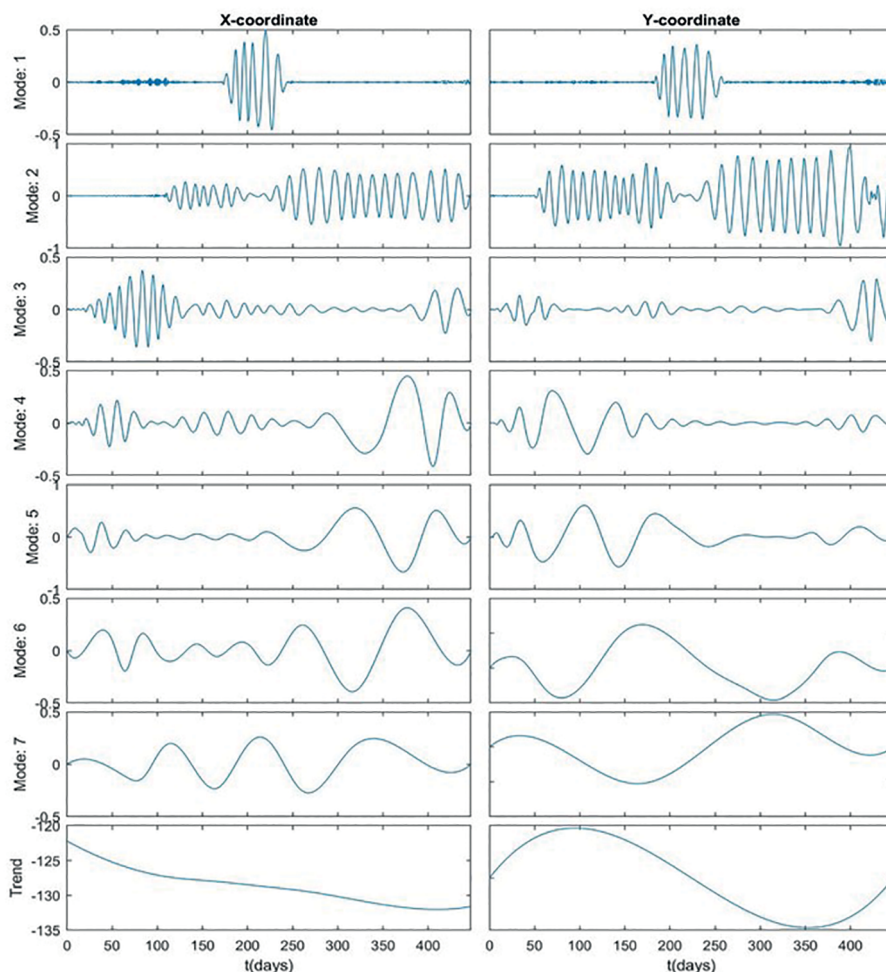


Figure 2. The IMFs and trend of (a) $x(t)$ and (b) $y(t)$ of the RAFOS float N073 from 21 November 1999 to 12 February 2001. Combination of IMF-1 to IMF-4 is the high-frequency component (eddy) and combination of IMF-5 to IMF-7 and the trend is the low-frequency component (i.e., mean flow).

low/non-low frequency ratio (see Appendix B). For RAFOS N073, combination of IMF-1 to IMF-4 is the high-frequency component (eddy) and combination of IMF-5 to IMF-7 and the trend is the low-frequency component (i.e., mean flow). After the separation of Lagrangian drifter's trajectory into deterministic and stochastic components with the total number of position points of J ,

$$\begin{aligned} x(t_j) &= x_{det}(t_j) + x_{sto}(t_j), \quad y(t_j) = y_{det}(t_j) + y_{sto}(t_j), \\ j &= 1, 2, \dots, J, \end{aligned} \quad (8)$$

the deterministic and stochastic velocities can be calculated from position vector (only showing x-direction) with the first-order difference for the two end points,

$$\begin{aligned} u_{sto}(t_1) &= \frac{x_{sto}(t_2) - x_{sto}(t_1)}{t_2 - t_1}, \quad u_{sto}(t_j) = \\ & \frac{x_{sto}(t_j) - x_{sto}(t_{j-1})}{t_j - t_{j-1}}, \end{aligned} \quad (9)$$

and the central difference for the internal points,

$$u_{sto}(t_j) = \frac{x_{sto}(t_{j+1}) - x_{sto}(t_{j-1})}{t_{j+1} - t_{j-1}}, \quad j = 2, 3, \dots, J-1. \quad (10)$$

Figure 3 shows the observed (red), deterministic (blue), and stochastic (green) trajectories of RAFOS N073. The deterministic trajectory represents the mean flow, i.e., the current. The stochastic trajectory indicates the eddy. The eddy is transported along the deterministic trajectory. The eddy in Figure 3 does not represent its real position and is separated from the deterministic trajectory arbitrarily just for illustration of eddy-like motion.

EDDY AND CUURENT CHARACTERISTICS IDENTIFIED FROM AN INDIVIDUAL RAFOS FLOAT

After the deterministic and stochastic trajectories and velocities are obtained from an individual RAFOS float, the eddy characteristics can be easily identified during the float 's drifting period. The eddy radial scale is defined by the root mean square of the stochastic trajectory

$$L_{eddy} = \sqrt{\frac{1}{J} \left[\sum_{j=1}^J \{ [x_{sto}^2(t_j) + y_{sto}^2(t_j)] \} \right]}. \quad (11)$$

The eddy velocity scale (V_{eddy}) is defined by

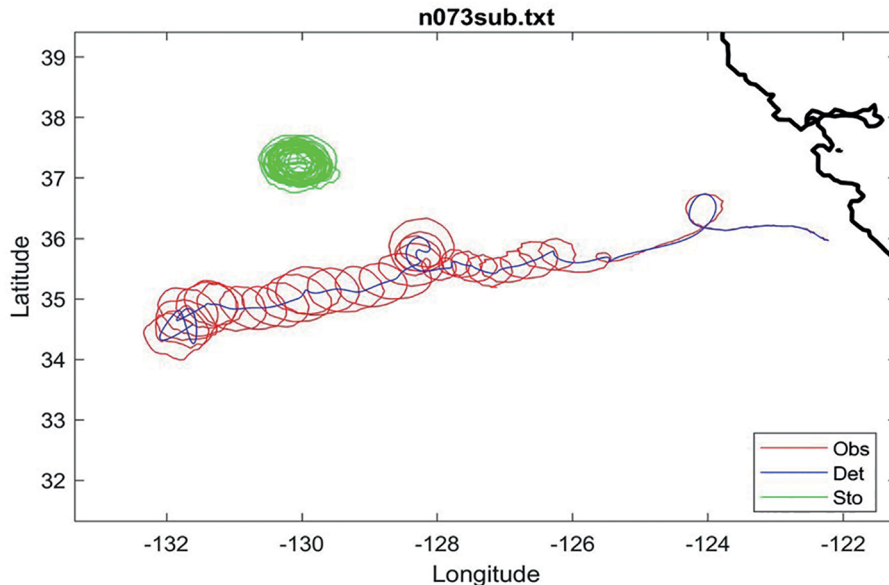


Figure 3. Observed (red), deterministic (blue), and stochastic (green) trajectories of RAFOS N073. The deterministic trajectory represents the mean flow. The stochastic trajectory indicates the eddy. The center of the eddy is transported by the mean flow (i.e., along the deterministic trajectory), and is put away from the deterministic trajectory arbitrarily just for illustration of eddy-like motion.

$$V_{eddy} = \sqrt{\frac{1}{J} \sum_{j=1}^J \left[\left(\frac{dx_{sto}(t_j)}{dt} \right)^2 + \left(\frac{dy_{sto}(t_j)}{dt} \right)^2 \right]} \quad (12)$$

The eddy velocity kinetic energy per unit mass, eddy angular velocity scale (Ω_{eddy}), and eddy Rossby number (R_{eddy}) are defined by

$$K_{eddy} = \frac{V_{eddy}^2}{2}, \quad \Omega_{eddy} = \frac{V_{eddy}}{L_{eddy}}, \quad R_{eddy} \equiv \frac{V_{eddy}}{fL_{eddy}} = \frac{\Omega_{eddy}}{f}, \quad (13)$$

where f is the Coriolis parameter, which is evaluated at 40oN here. The current velocity scale (V_{cur}) is defined by

$$V_{cur} = \sqrt{\frac{1}{J} \sum_{j=1}^J \left[\left(\frac{dx_{det}(t_j)}{dt} \right)^2 + \left(\frac{dy_{det}(t_j)}{dt} \right)^2 \right]} \quad (14)$$

Table 1 shows the current velocity scale and eddy characteristic parameters identified from the RAFOS floats with N073 float (21 November 1999 to 12 February 2001) as an example,

$$L_{eddy} = 36.53 \text{ km}, \quad V_{eddy} = 19.56 \text{ cm/s}, \quad R_{eddy} = 0.06, \quad V_{cur} = 8.38 \text{ cm/s}. \quad (15)$$

The current kinetic energy per unit mass (K_{cur}) and the eddy/current kinetic energy ratio (r) are defined by

$$K_{cur} = \frac{V_{cur}^2}{2}, \quad r = \frac{K_{eddy}}{K_{cur}} = \frac{V_{eddy}^2}{V_{cur}^2} \quad (16)$$

Due to eddy's circular motion (green trajectory in Figure 3), the time series of $[x_{sto}(t_j), v_{sto}(t_j)]$ or $[y_{sto}(t_j), u_{sto}(t_j)]$ determine the types of eddy (cyclonic or anticyclonic),

$$x_{sto}(t_j) > 0 \rightarrow \begin{cases} v_{sto}(t_j) > 0 \rightarrow \text{cyclonic} \\ v_{sto}(t_j) < 0 \rightarrow \text{anticyclonic} \end{cases} \quad (17)$$

$$x_{sto}(t_j) < 0 \rightarrow \begin{cases} v_{sto}(t_j) > 0 \rightarrow \text{anticyclonic} \\ v_{sto}(t_j) < 0 \rightarrow \text{cyclonic} \end{cases}$$

Table 2 shows the eddy-current kinetic energy ratio as well as the number of cyclonic/anticyclonic spirals. For the RAFOS float N073 float, we have

$$27 \text{ anticyclonic spirals}, \quad r = 5.45 \quad (18)$$

STATISTICS OF EDDY AND CURRENT CHARACTERISTIC PARAMETERS

Histograms of current velocity scale (V_{cur}) and eddy characteristic parameters such as radial scale (L_{eddy}), velocity scale (V_{eddy}), Rossby number (R_{eddy}), and eddy-current kinetic energy ratio (r) are constructed from 54 RAFOS floats shown in Tables 1 and 2. All the histograms are non-symmetric, high dispersive, and positively skewed (Figure 4). The California Undercurrent is an eddy-rich system [i.e., overall more kinetic energy for eddies than for currents with mean K_{eddy}/K_{cur} ratio of 1.78, standard deviation of 2.00, skewness of 2.79, and kurtosis 12.00 (Table 3). For N007 float (7 July – 5 September 1993), the eddy-current energy ratio is 0.13 with the eddy velocity scale of 6.91 cm/s and the current velocity scale of 19.16 cm/s, which is the minimum ratio to be observed. For N024 float (17 May – 9 June 1994), the eddy-current energy ratio is 11.18 with the eddy velocity scale of 33.94 cm/s and the current velocity scale of 10.15 cm/s, which is the maximum ratio to be observed. Besides, Table 3 shows the statistics of other eddy parameters. For example, the eddy radial scale (L_{eddy}) has a mean of 18.37 km, minimum of 1.12 km, maximum of 102.21 km, standard deviation of 21.33 km, skewness of 2.31, and kurtosis of 8.50. The eddy velocity scale has a mean of 11.98 cm/s, minimum of 2.72 cm/s, maximum of 44.17 cm/s, standard deviation of 8.65 cm/s, skewness of 1.74, and kurtosis of 5.82.

Among 54 RAFOS floats, 24 RAFOS floats (44%) represent the submesoscale eddies with $L_{eddy} < 10$ km (Table 1): 2.12, 6.88, 1.12, 7.98, 1.26, 0.90, 1.41, 6.09, 1.33, 9.26, 6.86, 1.38, 6.43, 9.45, 1.81, 2.56, 3.89, 2.42, 5.14, 3.81, 5.06, 6.48, 2.73, and 9.13 km, with a mean of 4.40 km and a standard deviation of 2.89 km. Their eddy velocity scales are 8.54, 9.80, 6.91, 10.08, 44.17, 29.22, 33.94, 10.99, 30.43, 3.43, 7.31, 4.74, 9.71, 8.32, 5.27, 4.99, 7.16, 6.28, 6.46, 8.02, 2.72, 6.13, 2.81, and 5.06 cm/s with a mean of 11.35 cm/s and a standard deviation of 11.04 cm/s. Their eddy Rossby numbers (R_{eddy}) are 0.45, 0.16, 0.70, 0.14, 3.99, 3.70, 2.76, 0.20, 2.61, 0.04, 0.12, 0.40, 0.15, 0.11, 0.33, 0.21, 0.20, 0.30, 0.14, 0.22, 0.06, 0.10,

Table 1. Identified current and eddy parameters from individual RAFOS float: radial scale (km), velocity scale (cm/s), and Rossby number.

Float	Buoy Days	dbar	L_{eddy} (km)	V_{cur} (cm/s)	V_{eddy} (cm/s)	R_{eddy}	Float	Buoy Days	dbar	L_{eddy} (km)	V_{cur} (cm/s)	V_{eddy} (cm/s)	R_{eddy}
N002	8/12-9/11/92	350	2.12	5.33	8.54	0.45	N050	8/29/96-1/9/98	275	25.95	8.08	8.40	0.03
N003	8/12-9/11/92	350	6.88	8.69	9.80	0.16	N051	2/25/97-7/8/98	275	102.21	6.91	9.54	0.01
N004	7/07-9/05/93	350	33.49	28.78	28.92	0.09	N053	9/11/97-8/22/98	275	10.75	8.52	12.14	0.12
N005	9/03/93-1/01/94	350	13.67	17.28	22.55	0.17	N055	9/11/97-8/22/98	275	6.86	10.12	7.31	0.12
N006	11/20/93-5/02/94	350	28.35	13.47	17.63	0.07	N062	4/29/98-6/25/99	275	1.38	6.72	4.74	0.40
N007	7/07-9/05/93	350	1.12	19.16	6.91	0.70	N063	5/17/98-7/12/99	275	18.56	6.06	4.94	0.03
N008	9/3-12/30/93	350	19.53	24.01	25.04	0.13	N064	4/29/98-6/25/99	275	6.43	7.51	9.71	0.15
N010	9/3/93-1/1/04	350	7.98	11.55	10.08	0.14	N065	4/29/98-6/24/99	275	9.45	4.19	8.32	0.11
N011	11/20/93-3/2/94	350	16.36	11.87	16.93	0.12	N066	10/27/98-12/23/99	275	13.59	8.79	7.14	0.06
N013	11/20/93-3/2/94	350	35.09	12.33	17.15	0.05	N067	10/27/98-12/23/99	275	20.21	7.93	13.76	0.07
N014	1/11-4/23/94	350	29.87	10.17	11.99	0.04	N069	5/5/99-5/18/00	275	1.81	6.65	5.27	0.33
N019	4/25-11/11/94	275	15.57	8.45	10.82	0.07	N071	5/5/99-5/18/00	275	2.56	5.10	4.99	0.21
N021	5/19-6/10/94	275	1.26	31.59	44.17	3.99	N072	11/21/99-2/12/01	275	3.89	6.29	7.16	0.20
N022	5/19-6/10/94	275	0.90	14.26	29.22	3.70	N073	11/21/99-2/12/01	275	36.53	8.38	19.56	0.06
N024	5/17-6/9/94	275	1.41	10.15	33.94	2.76	N075	11/21/99-2/12/01	275	2.42	14.14	6.28	0.30
N026	8/22-12/30/94	290	6.09	13.01	10.99	0.20	N080	7/26/00-9/23/01	275	5.14	8.97	6.46	0.14
N028	8/12-12/19/94	350	24.35	8.41	12.97	0.06	N081	7/26/00-5/22/02	275	28.13	8.13	6.89	0.03
N029	10/25/95-6/28/96	300	17.29	7.92	10.18	0.07	N082	7/26/00-9/24/01	275	3.81	10.44	8.02	0.22
N030	5/18-6/10/94	275	1.33	12.87	30.43	2.61	N083	9/11/00-12/29/01	275	15.04	7.49	13.37	0.10
N031	8/22-12/30/94	290	83.97	7.87	22.44	0.03	N084	9/11/00-7/9/02	275	5.06	5.70	2.72	0.06
N032	8/7/95-10/6/96	300	37.95	7.69	9.76	0.03	N085	9/11/00-7/9/02	275	12.91	11.33	7.13	0.06
N033	8/12/94-5/10/95	350	9.26	4.95	3.43	0.04	N087	5/20/01-11/6/02	275	6.48	8.21	6.13	0.10
N035	8/7/95-11/5/96	300	17.46	8.18	4.55	0.03	N088	5/20/01-7/28/03	275	22.00	6.43	7.02	0.03
N039	7/29/96-12/10/97	275	11.61	8.04	4.85	0.04	N089	5/20/01-7/28/03	275	17.10	6.70	7.30	0.05
N041	7/29/96-11/17/97	275	85.09	.666	10.95	0.01	N090	12/6/01-3/9/04	275	25.13	9.19	11.80	0.05
N043	2/25-12/13/97	275	57.07	10.34	11.59	0.02	N091	12/5/01-3/9/04	275	2.73	6.58	2.81	0.11
N048	7/29/96-9/19/97	275	11.43	7.09	7.37	0.06	N092	12/5/01-3/9/04	275	9.13	7.71	5.06	0.06

Table 2. Identified 36 cyclonic (denoted by ‘C’) spirals and 203 anticyclonic (denoted by AC) spirals and eddy to current kinetic energy ratio from 54 RAFOS floats.

Float	Buoy Days	Dbar	# of spirals	K_{eddy} / K_{cur} Ratio	Float	Buoy Days	dbar	# of spirals	K_{eddy} / K_{cur} Ratio
N002	8/12-9/11/92	350	C: 1	2.57	N050	8/29/96-1/9/98	275	AC: 1	1.08
N003	8/12-9/11/92	350	AC: 1	1.27	N051	2/25/97-7/8/98	275	AC: 3	1.91
N004	7/07-9/05/93	350	AC: 3	1.01	N053	9/11/97-8/22/98	275	C: 5	2.03
N005	9/03/93-1/01/94	350	AC: 2	1.70	N055	9/11/97-8/22/98	275	AC: 1	0.52
N006	11/20/93-5/02/94	350	AC: 2	1.71	N062	4/29/98-6/25/99	275	AC: 9	0.50
N007	7/07-9/05/93	350	AC: 5	0.13	N063	5/17/98-7/12/99	275	AC: 4	0.66
N008	9/3-12/30/93	350	AC: 2	1.09	N064	4/29/98-6/25/99	275	AC: 8	1.67
N010	9/3/93-1/1/04	350	C: 1	0.76	N065	4/29/98-6/24/99	275	C: 2	3.94
N011	11/20/93-3/2/94	350	AC: 3	2.03	N066	10/27/98-12/23/99	275	C: 6	0.66
N013	11/20/93-3/2/94	350	AC: 2	1.94	N067	10/27/98-12/23/99	275	AC:11	3.01
N014	1/11-4/23/94	350	C: 1	1.39	N069	5/5/99-5/18/00	275	AC: 1	0.63
N019	4/25-11/11/94	275	AC: 5	1.64	N071	5/5/99-5/18/00	275	AC: 5	0.95
N021	5/19-6/10/94	275	AC: 1	1.96	N072	11/21/99-2/12/01	275	AC: 7	1.30
N022	5/19-6/10/94	275	AC: 3	4.20	N073	11/21/99-2/12/01	275	AC:27	5.45
N024	5/17-6/9/94	275	AC: 5	11.18	N075	11/21/99-2/12/01	275	C: 1	0.20
N026	8/22-12/30/94	290	AC: 3	0.71	N080	7/26/00-9/23/01	275	AC:10	0.52
N028	8/12-12/19/94	350	AC: 5	2.38	N081	7/26/00-5/22/02	275	AC: 2	0.72
N029	10/25/95-6/28/96	300	AC: 1	1.65	N082	7/26/00-9/24/01	275	C: 4	0.59
N030	5/18-6/10/94	275	AC: 1	5.59	N083	9/11/00-12/29/01	275	AC: 9	3.18
N031	8/22-12/30/94	290	AC: 4	8.13	N084	9/11/00-7/9/02	275	C: 1	0.23
N032	8/7/95-10/6/96	300	C: 4	1.61	N085	9/11/00-7/9/02	275	AC: 5	0.40
N033	8/12/94-5/10/95	350	AC: 5	0.48	N087	5/20/01-11/6/02	275	C: 1	0.56
N035	8/7/95-11/5/96	300	C: 1	0.31	N088	5/20/01-7/28/03	275	AC: 5	1.19
N039	7/29/96-12/10/97	275	AC: 3	0.36	N089	5/20/01-7/28/03	275	AC: 4	1.19
N041	7/29/96-11/17/97	275	C: 1	2.70	N090	12/6/01-3/9/04	275	AC: 6	1.65
N043	2/25-12/13/97	275	AC: 3	1.26	N091	12/5/01-3/9/04	275	AC: 8	0.18
N048	7/29/96-9/19/97	275	C: 1	1.08	N092	12/5/01-3/9/04	275	C: 6	0.43

0.11, and 0.06 with the mean value of 0.72 and the standard deviation of 1.20.

The rest 30 RAFOS floats (56%) represent the mesoscale eddies with $L_{eddy} > 10$ km (Table 1): 33.49, 13.67, 28.35, 19.53, 16.36, 35.09, 29.87, 15.57, 24.35, 17.29, 83.97, 37.95, 17.46, 11.61, 85.09, 57.07, 11.43, 25.95, 102.21, 10.75, 18.56, 13.59, 20.21, 36.53, 28.13, 15.04, 12.91, 22.00, 17.10, and 25.13 km with a mean of 29.54 km and a standard deviation of 23.12 km. The eddy velocity scales (V_{eddy}) are 28.92, 22.55, 17.63, 25.04, 16.93, 17.15, 11.99, 10.82, 12.97, 10.18, 22.44,

9.76, 4.55, 4.85, 10.95, 11.59, 7.37, 8.40, 9.54, 12.14, 4.94, 7.14, 13.76, 19.56, 6.89, 13.37, 7.13, 7.02, 7.30, and 11.80 cm/s with a mean of 12.49 cm/s and a standard deviation of 6.28 cm/s. The eddy Rossby numbers (R_{eddy}) are 0.09, 0.17, 0.07, 0.13, 0.12, 0.05, 0.04, 0.07, 0.06, 0.07, 0.03, 0.03, 0.03, 0.04, 0.01, 0.02, 0.06, 0.03, 0.01, 0.12, 0.03, 0.06, 0.07, 0.06, 0.03, 0.10, 0.06, 0.03, 0.05, and 0.05 with a mean of 0.06 and a standard deviation 0.04. The overall eddy velocity scales are comparable between the submesoscale eddies (mean: 11.35 cm/s, standard deviation: 11.04 cm/s) and

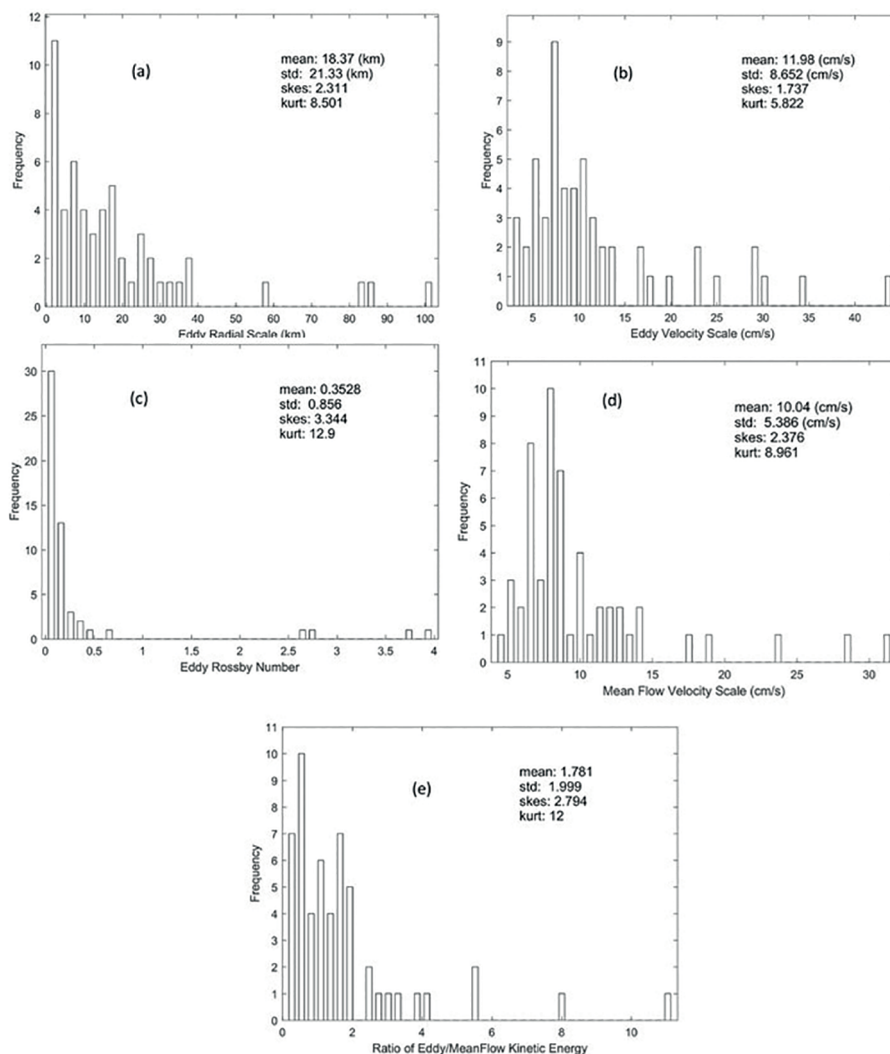


Figure 4. Histograms of current and eddy characteristic parameters identified from 54 RAFOS floats: (a) eddy radial scale (km), (b) eddy velocity scale (cm/s), and (c) eddy Rossby number, (d) current velocity scale (cm/s), and (e) eddy and current kinetic energy ratio.

the mesoscale eddies (mean: 12.49 cm/s, standard deviation: 6.28 cm/s). This may imply that the California Undercurrent has submesoscale and mesoscale eddies and 10 km is a good threshold of the eddy radial scale (L_{eddy}) to separate the two. The eddy Rossby numbers are more than an order of magnitude larger for the submesoscale eddies (mean: 0.72, standard deviation: 1.20) than for the mesoscale eddies (mean: 0.06, standard deviation: 0.04).

The eddy-current kinetic energy ratio (Table 3) ratios are 2.57, 1.27, 0.13, 0.76, 1.96, 4.20, 11.19, 0.71, 5.59, 0.48, 0.52, 0.50, 1.67, 3.94, 0.63, 0.95, 1.30, 0.20, 0.52, 0.59, 0.23, 0.56, 0.18, and 0.43

for $L_{eddy} < 10$ km, representing submesoscale eddies, with a mean of 1.71 and a standard deviation of 2.47. The eddy-current kinetic energy ratios are 1.01, 1.70, 1.71, 1.09, 2.03, 1.94, 1.39, 1.64, 2.38, 1.65, 8.13, 1.61, 0.31, 0.36, 2.70, 1.26, 1.08, 1.08, 1.91, 2.03, 0.66, 0.66, 3.01, 5.44, 0.72, 3.18, 0.40, 1.19, 1.19, and 1.65 for $L_{eddy} > 10$ km, representing mesoscale eddies, with a mean of 1.84 and a standard deviation of 1.57 for the rest 30 floats. Both mean and standard deviation are comparable for the submesoscale and mesoscale eddies. This may imply that the current-eddy kinetic energy transfer is similar for submesoscale and mesoscale eddies.

TEMPORAL VARIABILITY OF EDDY AND CURRENT CHARACTERISTIC PARAMETERS

All the identified eddy and current parameters (L_{eddy} , V_{eddy} , R_{eddy} , V_{cur} , r) have evident temporal variabilities (Figure 5). Large dispersion is found in L_{eddy} before August 1998 from 1.12 km (7 July – 5 September 1993, N007) to 102.21 km (25 February 1997 – 8 July 1998, N051). Small dispersion in L_{eddy} is found after August 1998 with a maximum of 36.53 km (21 November 1999 – 12 February 2001, N073) (Figure 5a) and a minimum of 1.81 km (5 May 1999 – 18 May 2000, N069). Large dispersion is found in V_{eddy} before 1995 from 6.91 cm/s (7 July – 5 September 1993, N007) to 44.17 cm/s (19 May – 10 June 1994, N021). Small

dispersion is found after December 1994 with a maximum of 19.56 cm/s (21 November 1999 – 12 February 2001, N073) and a minimum of 2.72 cm/s (11 September 2000 – 9 July 2002, N084) (Figure 5b). The eddy Rossby number (R_{eddy}) is mostly less than 0.5 (Figure 5c). Large disperse is found before 1995 with large values of 3.99 (N021), 3.70 (N022), 2.76 (N024), during 17 May – 10 June 1994 and 18 May-10 June 1994 and small value of 0.03 during 7 August – 30 December 1994 (N031). Small dispersion is found after 1995 with a maximum of 0.33 during 5 May 1999 - 18 May 2000 (N069) (Figure 5c). The current velocity scale (V_{cur}) has larger dispersion before 1995. It has a maximum of 31.59 cm/s during 19 May – 10 June 1994 (N021) and a minimum of 5.33 cm/s during 12 August – 11 September 1992 (N002). It has smaller dispersion

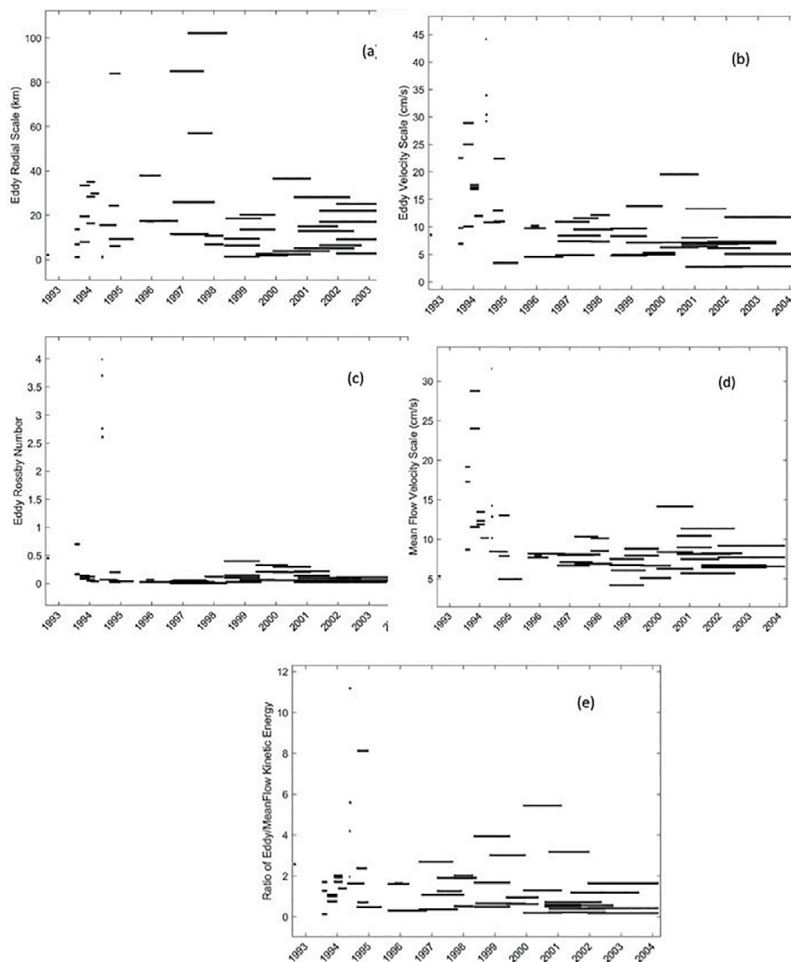


Figure 5. Temporal variation of identified current and eddy characteristic parameters from 54 RAFOS floats: (a) eddy radial scale (km), (b) eddy velocity scale (cm/s), and (c) eddy Rossby number, (d) current velocity scale (cm/s), and (e) eddy and current kinetic energy ratio.

after 1995 with a maximum of 14.14 cm/s during 21 November 1999 – 12 February 2001 (N075) and a minimum of 4.19 cm/s during 29 April 1998 – 24 June 1999 (N065) (Figure 5d). The K_{eddy}/K_{cur} ratio has larger dispersion before 1995 with a maximum of 11.18 during 17 May – 9 June 1994 (N024) and a minimum of 0.13 during 7 July – 5 September 1993 (N007). It has smaller dispersion after 1995 with a maximum of 5.45 during 21 November 1999 – 12 February 2001 (N073) and a minimum of 0.23 values during 11 September 2000 – 9 July 2002 (N084) (Figure 5e).

CONCLUSION

The deterministic-stochastic EMD is used to decompose a RAFOS float trajectory. Time differentiation of the deterministic and stochastic trajectories leads to the Lagrangian current and eddy velocities. Application of this method to analysis of 54 RAFOS floats deployed by NPS from 1992 to 2004 at depth between 150 and 600 m leads to the fact that the California Undercurrent is an eddy-rich system with the overall eddy-current kinetic energy ratio of 1.78. These eddies are mostly anticyclonic with total 203 anticyclonic and 36 cyclonic spirals. Both submesoscale and mesoscale eddies exist with the mean eddy Rossby number of 0.72 for the submesoscale eddies and 0.06 for the mesoscale eddies. The overall eddy velocity scales are comparable between the submesoscale eddies (mean: 11.35 cm/s) and the mesoscale eddies (mean: 12.49 cm/s). The current-eddy kinetic energy transfer is similar between the two. The horizontal length scale of 10 km is a good threshold of the eddy radial scale (L_{eddy}) to separate the submesoscale and mesoscale eddies.

The identified eddy and current parameters (L_{eddy} , V_{eddy} , R_{eddy} , V_{cur} , r) have evident temporal variabilities. Large dispersion is found in L_{eddy} before August 1998 and small dispersion in L_{eddy} is found after August 1998. Large dispersion of (V_{eddy} , R_{eddy} , V_{cur} , r) is found before 1995 and small dispersion is found after 1995. Further studies are needed on physical mechanisms to cause such a temporal variability.

ACKNOWLEDGMENTS

It is our pleasure to contribute to a special volume honoring Professor Afonso Mascarenhas. He was a visiting professor at NPS through the National Research Council Senior Visitor Program during October 2006 – March 2007. The authors learned a lot from him on the circulation in the Gulf of California. Besides, the authors would like to thank Professor (emeritus) Curt Collins at NPS for collecting RAFOS data and unselfishly posting the data at the website.

AUTHOR CONTRIBUTIONS

P.C.C.: Conceptualization; Investigation; Methodology; Writing – original draft, review & editing.

C.F.: Methodology; Graphics.

REFERENCES

- BAUER, S., SWENSON, S., GRIFFA, A., MARIANO, A. J. & OWENS, K. 1998. Eddy-mean decomposition and eddy-diffusivity estimates in the tropical Pacific Ocean. *Journal of Geophysical Research*, 103(C13), 855-871.
- CHU, P. C. 2018. Steepest ascent low/non-low frequency ratio in empirical mode decomposition to separate deterministic and stochastic velocities from a single Lagrangian drifter. *Journal of Geophysical Research*, 123(3), 1708-1721, DOI: <https://doi.org/10.1002/2017JC013500>
- CHU, P. C. & FAN, C. W. 2014. Accuracy progressive calculation of Lagrangian trajectory from gridded velocity field. *Journal of Atmospheric and Oceanic Technology*, 31(7), 1615-1627.
- CHU, P. C., FAN, C. W. & HUANG, N. 2012. Compact empirical mode decomposition — an algorithm to reduce mode mixing, end effect, and detrend uncertainty. *Advances in Adaptive Data Analysis*, 4(3), 1250017, DOI: <https://doi.org/10.1142/S1793536912500173>
- CHU, P. C., FAN, C. W. & HUANG, N. 2014. Derivative-optimized empirical mode decomposition for the Hilbert-Huang transform. *Journal of Computational and Applied Mathematics*, 259(Pt A), 57-64.
- CHU, P. C., IVANOV, L. M., KORZHOVA T. P., MARGOLINA, T. M. & MELNICHENKO, O. M. 2003a. Analysis of sparse and noisy ocean current data using flow decomposition. Part 1: theory. *Journal of Atmospheric and Oceanic Technology*, 20(4), 478-491.
- CHU, P. C., IVANOV, L. M., KORZHOVA T. P., MARGOLINA, T. M. & MELNICHENKO, O. M. 2003b. Analysis of sparse and noisy ocean current data using flow decomposition. Part 2: application to Eulerian and Lagrangian data. *Journal of Atmospheric and Oceanic Technology*, 20, 492-512.

- CHU, P. C., IVANOV, L. M. & MELNICHENKO, O. M. 2005. Fall-winter current reversals on the Texas-Louisiana continental shelf. *Journal of Physical Oceanography*, 35, 902-910.
- CHU, P. C., IVANOV, L. M., MELNICHENKO, O. V. & WELLS, N. C. 2007. On long baroclinic Rossby waves in the tropical North Atlantic observed from profiling floats. *Journal of Geophysical Research*, 112(C5), C05032, DOI: <https://doi.org/10.1029/2006JC003698>
- COLLINS, C. A., GARFIELD, N., RAGO, T. A., RISERMILLER, F. W. & CARTER, E. 2000. Mean structure of the inshore countercurrent and California Undercurrent off Point Sur, California. *Deep Sea Research Part II*, 47, 765-782.
- COLLINS, C. A., IVANOV, L. M., MELNICHENKO, O. B. & GARFIELD, N. 2004. California Undercurrent variability and eddy transport estimated from RAFOS float observations. *Journal of Geophysical Research*, 109(C5), DOI: <https://doi.org/10.1029/2003JC002191>
- COLLINS, C. A., PAQUETTE, R. G. & RAMP, S. R. 1996. *Annual variability of ocean currents at 350m depth over the continental slope off Point Sur, California, CalCOFI Report, 37*. La Jolla: California Cooperative Oceanic Fisheries Investigations, pp. 257-263.
- DAVIS, R. E. 1991. Observing the general circulation with floats. *Deep Sea Research*, 38(Suppl 1), S531-S571.
- GARFIELD, N., COLLINS, C. A., PAQUETTE, R. G. & CARTER, E. 1999. Lagrangian exploration of the California undercurrent, 1992-95. *Journal of Physical Oceanography*, 29, 560-583.
- HUANG, N., SHEN, Z., LONG, S. R. WU, M. C., SMITH, H. H., ZHENG, Q., YEN, N., TUNG, C. C. & LIU, H. H. 1998. The empirical mode decomposition and the Hilbert spectrum for nonlinear and non-stationary time series analysis. *Proceedings of Royal Society London*, 454, 903-995.
- HUYER, A., BARTH, J. A., KOSRO, P. M., SHEARMAN, R. K. & SMITH, R. L. 1998. Upper-ocean water mass characteristics of the California Current, summer 1993. *Deep Sea Research Part II: Topical Studies in Oceanography*, 45(8-9), 1411-1442.
- OBUKO, A. & EBBESMEYER, C. C. 1976. Determination of vorticity, divergence, and deformation rates from analysis of drogue observations. *Deep Sea Research and Oceanographic Abstracts*, 23(4), 349-352.
- RIOS, R. A. & MELLO, R. F. 2016. Applying empirical mode decomposition and mutual information to separate stochastic and deterministic influences embedded in signals. *Signal Processing*, 118, 159-176.
- RYPINA, I. I., KAMENKOVICH, I., BERLOFF, P. & PRATT, L. J. 2012. Eddy-induced particle dispersion in the near-surface North Atlantic. *Journal of Physical Oceanography*, 42(12), 2206-2228.
- SIMPSON, J. J. & LYNN, R. J. 1990. A mesoscale eddy dipole in the off-shore California Current. *Journal of Geophysical Research*, 95(C8), 13009-13022.

APPENDIX A. EMPIRICAL MODE DECOMPOSITION

This appendix is duplicated from Section 2 of Chu et al. [2012]. Let $x(t)$ represent the time series with fluctuations on various time scales [see Fig. A1]. The empirical mode decomposition (EMD) method is depicted as follows. First, the local minima and maxima of the signal $x(t)$ are identified. Second, the local maxima are connected together by interpolation, forming an upper envelope $e_{max}(t)$. The same is done for local minima, providing a lower envelope $e_{min}(t)$. Third, the mean of the two envelopes are calculated

$$m_1(t) = [e_{max}(t) + e_{min}(t)]/2. \tag{A1}$$

Fourth, the mean is subtracted from the signal, providing the local detail

$$h_1(t) = x(t) - m_1(t). \tag{A2}$$

The time series $h_1(t)$ is checked if it has local minima and local maxima. If yes, $h_1(t)$ is considered as the first IMF and denoted

$$c_1(t) = h_1(t). \tag{A3}$$

It is subtracted from the original signal and the first residual,

$$r_1(t) = x(t) - h_1(t), \tag{A4}$$

is taken as the new series in step 1. If $h_1(t)$ is not an IMF, a procedure called “sifting process” is applied as many times as necessary to obtain an IMF. In the sifting process, $h_1(t)$ is considered as the new data, and the same procedure applies. The IMFs are orthogonal, or almost orthogonal functions (mutually uncorrelated). Because this method does not require stationarity and linearity of the data and is especially suitable for nonstationary and nonlinear time series analysis.

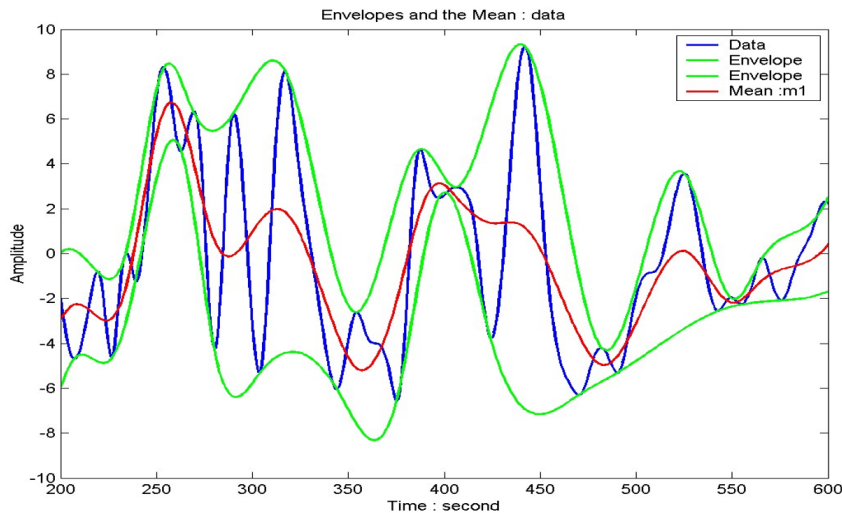


Figure A1. Procedure of the empirical mode decomposition (EMD).

By construction, the number of extrema decreases when going from one residual to the next. The application of the above algorithm ends when the residual has only one extrema, or is constant. In this case

no more IMF can be extracted. The complete decomposition is then achieved in a finite number of steps. The signal $c(t)$ is finally written as the sum of IFMs $c_p(t)$ and the trend $r(t)$:

$$c(t) = \sum_{p=1}^P c_p(t) + r(t) , \quad (\text{A5})$$

where $c(t)$ represents $x(t)$ and $y(t)$. There is no any oscillation (i.e., non-existence of both maximum and minimum envelopes) in the trend $r(t)$, which should represent the trend. Obviously, successfulness of the EMD depends on accurate determination of upper and lower envelopes.

APPENDIX B. STEEPEST ASCENT LOW/HIGH FREQUENCY RATIO

To separate $c(t)$ into deterministic and stochastic components, we have to determine the s -th IMF mode, in which the stochastic signal combination of the 1st, 2nd, ..., s -th IFMs constitutes, and the combination of $(s+1)$ -th, $(s+2)$ -th, ..., P -th IFMs. The trend constitutes the deterministic signal. To do so, the Fourier transform is conducted on each IMF $c_p(t)$:

$$f_{pk} = \frac{1}{J} \sum_{j=0}^{J-1} c_p(t_j) \exp\left[(-i2\pi k / J)t_j\right], \quad k = 0, 2, \dots, J-1 \quad (\text{B1})$$

which is a set of complex coefficients in the frequency space. Here, $i \equiv \sqrt{-1}$ and J is the length of the time series. For each IFM $c_p(t)$, the phase spectrum (Rios and de Mello 2016; Chu 2018) is calculated by

$$\theta_p(k) = \arctan \frac{\text{Im}(f_{pk})}{\text{Re}(f_{pk})} \quad (\text{B2})$$

and the amplitude is computed up to the Nyquist frequency

$$a_p(k) = \sqrt{|f_{pk} \hat{f}_{pk}|} / J, \quad k = 1, 2, \dots, J/2. \quad (\text{B3})$$

Let m represent lowest α -fraction ($\alpha < 1$) of the frequency domain, i.e., $m = [\alpha \times J / 2]$ with the bracket indicating the integer part. The powers of lowest α -fraction frequency ($E_{p,\alpha}$) and total frequency (E_p) are defined by (Chu 2018):

$$E_{p,\alpha} = \sum_{k=1}^m a_p^2(k), \quad E_p = \sum_{k=1}^{J/2} a_p^2(k). \quad (\text{B4})$$

The low/non-low frequency ratio is defined by

$$R_{p,\alpha} = \frac{E_{p,\alpha}}{E_p - E_{p,\alpha}}, \quad (\text{B5})$$

which indicates the low frequency (α -fraction) dominance of the p -th IMF. The s -th IMF mode is determined by the ratio of the low frequency dominance parameter for the $(p+1)$ -th IMF to the p -th IMF

$$\Gamma_{p,\alpha} = \frac{R_{p+1,\alpha}}{R_{p,\alpha}}, \quad (\text{B6})$$

which represents increase of strength of the low frequency component. Since the low frequency enhances as the mode number p increases, separation of deterministic and stochastic signals is at the IMF with the maximum value of the ratio

$$\Gamma_{s,\alpha} = \max(\Gamma_{p,\alpha} \mid p = 1, 2, \dots, P-1). \quad (\text{B7})$$

The combination of the 1st, 2nd, ..., s -th IFMs constitutes the stochastic signal, and the combination of $(s+1)$ -th, $(s+2)$ -th, ..., P -th IFMs, and the trend constitutes the deterministic signal.